View metadata, citation and similar papers at core.ac.uk

brought to you by CORE

provided by Explore Bristol Research

Du, B., Tang, C., Zhao, D., Zhang, H., Yu, D., Yu, M., Coimbatore Balram, K., Gersen, H., Yang, B., Cao, W., Gu, C., Besenbacher, F., Li, J., & Sun, Y. (2019). Diameter-optimized high-order waveguide nanorods for fluorescence enhancement applied in ultrasensitive bioassays. *Nanoscale*, 14322-14329. https://doi.org/10.1039/C9NR02330E

Peer reviewed version

License (if available):
Other

Link to published version (if available):
10.1039/C9NR02330E

Link to publication record in Explore Bristol Research
PDF-document

This is the accepted author manuscript (AAM). The final published version (version of record) is available online via The Royal Society of Chemistry at https://doi.org/10.1039/C9NR02330E . Please refer to any applicable terms of use of the publisher.

University of Bristol - Explore Bristol Research

General rights

This document is made available in accordance with publisher policies. Please cite only the published version using the reference above. Full terms of use are available:
http://www.bristol.ac.uk/red/research-policy/pure/user-guides/ebr-terms/

Nanoscale

PAPER

Diameter-optimized high-order waveguide nanorods for fluorescence enhancement applied in ultrasensitive bioassays

Received 00th January 20xx,
Accepted 00th January 20xx

DOI: 10.1039/x0xx00000x

Baosheng Du,[a, c] Chengchun Tang,[b] Dan Zhao,[f] Hong Zhang,[a] Dengfeng Yu,[a,c] Miao Yu,*[c] Krishna C. Balram,[d] Henkjan Gersen,[e] Bin Yang,[a] Wenwu Cao,[a] Changzhi Gu,[b] Flemming Besenbacher,*[g] Junjie Li*[b] and Ye Sun*[a]

Development of fluorescence enhancement (FE) platforms based on ZnO nanorods (NRs) has sparked considerable interest, thanks to their well-demonstrated potential in chemical and biological detection. Among the multiple factors determining the FE performance, high-order waveguide modes are specifically promising in boosting the sensitivity and realizing selective detection. However, quantitative experimental studies on the influence of the NR diameter, substrate, and surrounding medium, on the waveguide-based FE properties remain lacking. In this work, we have designed and fabricated a FE platform based on patterned and well-defined arrays of vertical, hexagonal prism ZnO NRs with six distinct diameters. Both direct experimental evidence and theoretical simulations demonstrate that high-order waveguide modes play a crucial role in FE, and are strongly dependent on the NR diameter, substrate, and surrounding medium. Using the optimized FE platform, a significant limit of detection (LOD) of 10^{-16} mol L^{-1} for Rhodamine-6G probe detection is achieved. Especially, a LOD as low as 10^{-14} g mL^{-1} is demonstrated for a prototype biomarker of carcinoembryonic antigen, which is improved by one order compared with the best LOD ever reported using fluorescence-based detection. This work provides an efficient path to design waveguiding NRs-based biochips for ultrasensitive and highly-selective biosensing.

Introduction

Fluorescence-based detection and analysis plays an important role in the fields of biology, medical science, environmental monitoring and food safety detection, as these approaches are quantifiable, simple to use, versatile, and above all practical.[1–9] Further improvement in sensitivity and realizing selective detection of multi-components remain highly desirable yet challenging for applications, *e.g.* diagnosis of early-stage cancer in clinic.[10–12] To accomplish high detection sensitivity, diverse organic dyes and inorganic nanoparticles with high quantum yields have been utilized as fluorescent probes.[13–21] Considering that the quantum yields of such probes are already > 75%,[19–21] further improvement by employing advanced fluorescent probes appears rather limited. An alternative and far more promising strategy to address this challenge would be to develop novel fluorescence enhancement (FE) platforms, which lately have sparked enormous interest.[22–30]

A big variety of FE platforms, including silver nanoparticles, gold nanoparticles/nanorods (NRs), Si/SiO_2 nanopillars, GaP nanowires, ZnO NRs, *etc.* have been successfully fabricated and studied.[22–36] Amongst them, ZnO NRs-based FE platforms are particularly fascinating in bioassays, thanks to their well-recognized benefits, such as prevention from fluorescence quenching, no optical absorption in the entire visible to near-infrared region, relatively large refractive index, controllable morphology and alignment, facile fabrication, and low cost.[37–40] It is therefore no surprise that enormous effort has been devoted to improve the detection performance of ZnO NRs-based FE platforms through various morphology and surface/interface modification.[30,37,38,41–43] For instance, a low limit of detection (LOD) of 100 fg mL^{-1} for carcinoembryonic antigen (CEA), a typical cancer biomarker, was achieved through coating ZnO NRs with a polymer layer to enhance protein loading capacity[42] or integrating ZnO NRs within special designed microfluidic chips.[43]

Besides increasing the surface area and biomolecule binding properties, which determine the phosphors loading capability of the FE platform,[42,44] waveguiding effects of ZnO NRs, which has been widely applied in nano-lasers, sensors, *etc.*,[45–47] are predicted to have a significant impact on their FE performance.[30,37,38,48,49] The fundamental waveguide mode is suggested to capture and guide

[a] *Condensed Matter Science and Technology Institute, School of Instrumentation Science and Engineering, Harbin Institute of Technology, Harbin 150080, China. E-mail: sunye@hit.edu.cn.*
[b] *Beijing National Laboratory for Condensed Matter Physics, Institute of Physics, Chinese Academy of Sciences, Beijing 100190, China. E-mail: jjli@iphy.ac.cn.*
[c] *State Key Laboratory of Urban Water Resource and Environment, School of Chemistry and Chemical Engineering, Harbin Institute of Technology, Harbin 150001, China. E-mail: miaoyu_che@hit.edu.cn.*
[d] *QET Labs, Department of Electrical & Electronic Engineering, University of Bristol, Bristol, BS8 1UB, United Kingdom*
[e] *Nanophotonics and Nanophysics Group, H. H. Wills Physics Laboratory, University of Bristol, Bristol, BS8 1TL, United Kingdom*
[f] *National Key Laboratory of Tunable Laser Technology, Harbin Institute of Technology, Harbin 150001, China*
[g] *iNANO and Department of Physics and Astronomy, Aarhus University, Aarhus 8000, Denmark. E-mail: fbe@inano.au.dk*
Electronic Supplementary Information (ESI) available: Fluorescence enhancement properties of the ZnO nanorods without the Au layer, and supporting figures. See DOI: 10.1039/x0xx00000x

Please do not adjust margins

the fluorescence signal,[37,38,47] whilst the higher-order waveguide modes provide a strong evanescent field outside the ZnO NR, that can greatly enhance the excitation of any phosphors adjacent to the NRs.[30,37,38,50] It has been theoretically suggested that the evanescent field is strongly dependent on the diameter (*d*) of the NRs.[51] Following this logic, precisely adjusting *d* could therefore be an effective way to enhance the fluorescence detection sensitivity of ZnO NRs-based platforms. Based on theoretical simulations,[51] vertical and highly crystalline ZnO NRs with controlled *d* in the scale of several hundred nanometers are appropriate models to reveal the impact of high-order waveguide modes on FE performance of ZnO NRs. However, most reported ZnO NRs employed in FE platforms present less-controlled diameter, alignment and distribution, which have restricted the FE performance and the possibility to quantitatively explore the influence of waveguiding properties on FE.[30,37–39,42,43] A recent report of the ZnO NRs on FE demonstrated that increased *d* hence reduced gap between the neighbouring NRs can contribute to strong interactions between evanescent fields of NRs.[52] However, these *d* values in the range of 40−85 nm are too small to generate strong evanescent field.

Effect of diameter on FE properties of vertical Si nanopillars[34,35] and GaP nanowires[36] have been explored, revealing that the diameter-dependent waveguiding properties can modifiy not only the FE performance but also the fluorescence intensity profiles along the nanowire axial direction. However, the relatively stronger visible light absorption of these Si nanopillars and GaP nanowires and the remaining coating materials on the tops of Si and GaP nanomaterials can hinder the incidence of the excitation light into the NRs from the top direction and compromise the formation of the excitation light-related evanescent field. Therefore, a direct FE properties comparasion of ZnO NRs with these nanowires/nanopillars are not plausible. Moreover, additional factors, such as the substrate and surrounding medium, could also play a role in the FE properties of the NRs platform. However, the related study remains lacking. A quantative experimental and theoretical investigation on the effect of NR diameter, substrate, and surrounding medium on waveguiding properties is highly preferred for both in-depth understanding of its contribution to FE and rational optimizing FE platforms, holding great promise for selective fluorescence detection.

Herein, patterned arrays of vertical hexagonal prism ZnO NRs with precisely-controlled diameter, height and lateral arrangement have been achieved with the aid of microfabrication (Scheme 1). Six types of arrays composed of NRs with different *d* are simultaneously fabricated on a substrate pre-coated with an Au-layer. The experimental results and the finite-difference time-domain (FDTD) simulations demonstrate that high-order waveguide modes play a crucial role in the FE performance of ZnO NRs, and that optimizing *d*, applying high-reflection substrate and tuning the surrounding medium can efficiently improve the fluorescence detection sensitivity. Remarkably, a LOD as low as 0.1 fM for Rhodamine-6G (R6G) probe and an ultralow LOD of 10 fg mL^{-1} for Cyanine-3 (Cy3)-based CEA fluorescence detection are achieved. The latter is one order of magnitude improved than the best reported results based on fluorescence-based detection,[42,43,53–55] highlighting the significant potential of this platform for ultrasensitive bioassays.

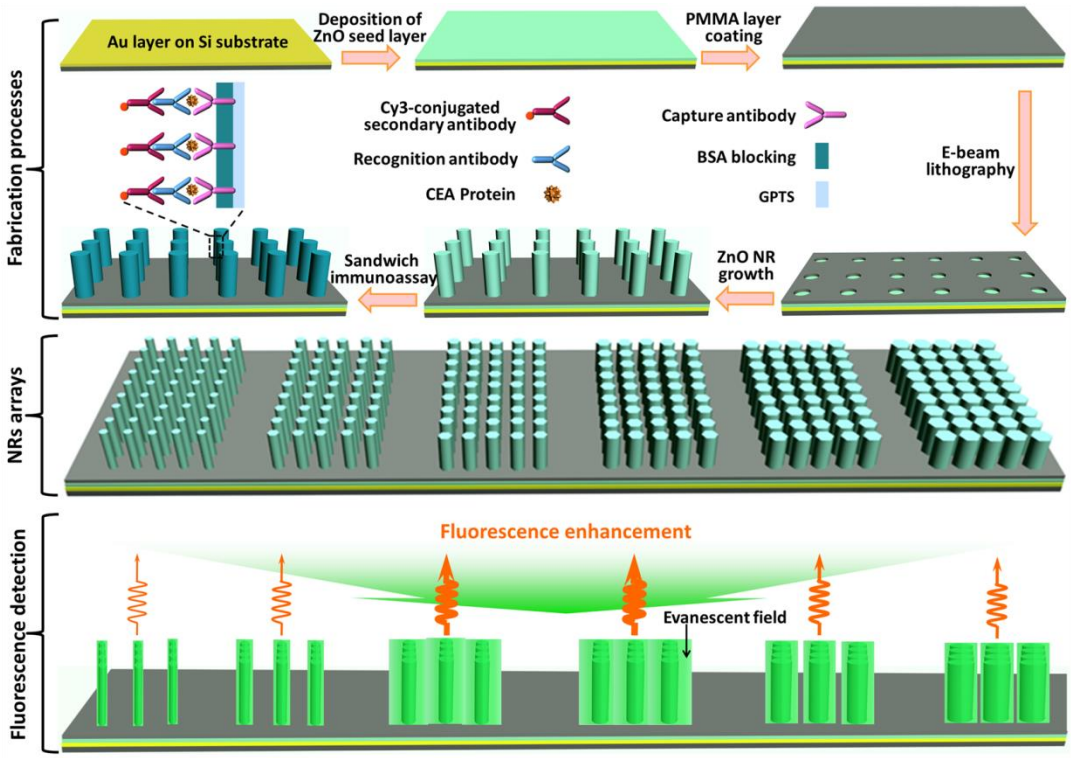

Scheme 1. Schematic illustration for the fabrication and fluorescence-enhanced detection of the ZnO NRs-based platform.

This journal is © The Royal Society of Chemistry 20xx

Please do not adjust margins

Please do not adjust margins

Experimental

Materials

Zinc nitrate hexahydrate, hexamethylenetetramine, (3-glycidoxy propyl) trimethoxysilane (GPTS), glycerol, Triton ®X-100, 0.01 M PBS (pH 7.4), 0.05 mol L^{-1} tris buffered saline containing 0.05% Tween®20 (TBS, PH 8.0), bovine serum albumin (BSA), and R6G were purchased from Aladdin (China). The target biomarker of CEA, capture antibody of monoclonal mouse anti-CEA (CEA-mAb), recognition antibody of polyclonal rabbit anti-CEA (CEA-pAb), and Cy3-labelled secondary antibody of goat anti rabbit IgG were purchased from Abcam (China).

Fabrication of ZnO NRs arrays

An Au layer was deposited on a Si substrate by radio frequency magnetron sputtering for 10 min at room temperature in vacuum. Sequentially, ceramic ZnO target was sputtered for 30 min at 400 °C with an Ar/O_2 atmosphere (flow rates of Ar and O_2 are 40 sccm and 10 sccm, respectively) at a pressure of 1 Pa to coat a <002>-oriented ZnO seed layer on the Au layer.

In order to precisely control the size and lateral distribution of the ZnO NRs arrays, a ~200 nm thick polymethyl methacrylate (PMMA) mask layer was spin-coated on the ZnO seed layer, and then arrays of circular apertures with defined distribution and six different diameters (*ca.* 100, 150, 200, 250, 300 and 400 nm) were etched using an electron beam lithography technique.

Well-aligned ZnO NRs were then grown from the ZnO seed layer exposed at the bottom of the circular apertures by a modified hydrothermal method with zinc nitrate and hexamethylenetetramine as the precursors.[56,57] In short, zinc nitrate solution (50 mL, 20 mM) and hexamethylenetetramine solution (50 mL, 20 mM) were heated separately at 70 °C for 30 min and then mixed together in a glass bottle. After immersing the PMMA/ZnO seed layer sample into the solution, the glass bottle was immediately sealed and maintained at 70 °C for 8 h. The resulted NR samples were rinsed with deionized water and then dried under a gentle flow of nitrogen gas. For convenience, the NRs arrays on Au layer were denoted as '*AZ1*', '*AZ2*', '*AZ3*', '*AZ4*', '*AZ5*', and '*AZ6*', respectively, according to the etched aperture sizes from the minimum (~100 nm) to the maximum (~400 nm).

Characterizations

The samples were characterized by scanning electron microscope (SEM, FEI, Quanta 200F), atomic force microscopy (Bruker, Multimode 8), X-ray diffraction (Bruker, Advanced D8, with Cu Kα radiation), Fourier transform infrared spectrometer (FTIR, Nicolet 6700, Thermo Scientific), and fluorescence spectrometer (Fluoro Max-4-TCSPC, Horiba Jobin Yvon).

Fluorescence enhancement properties

After immersion in R6G solutions (10 mL) at different concentrations and 4 °C for 24 h, the samples were thoroughly washed by deionized water and then dried in air before characterization by a fluorescence microscope (Leica, DM4000 B using excitation light at 530±20 nm). All fluorescent images were collected under the same conditions with a fixed exposure time of 1 s, and quantitatively analysed by the Leica AF software.

CEA detection

A sandwich immunoassay method was applied to the NR samples to explore the influence of their FE performance on CEA detection. In short, the NR samples were first incubated with 5% (*V*/*V*) GPTS ethanol solution for 3h. After curing in vacuum at 110 °C for 2 h, the samples were then incubated with the solution of CEA-mAb (200 μg mL^{-1}) containing 0.01 M PBS, 2.5% glycerol and 0.004% Triton X-100. Following incubation at room temperature for 12 h, the samples were blocked with 1% BSA solution for 1h to eliminate the nonspecific binding of proteins, and then washed with 0.05 M TBS. Afterwards, the samples were incubated with CEA solutions at different concentrations (1 fg mL^{-1}–1 μg mL^{-1}) containing 10% human serum for 1 h. After rinsing with TBS, they were allowed to sequentially react with the recognition antibody of Rabbit anti-CEA (500-fold dilution) for 1 h and 5 μg mL^{-1} Cy3-labelled anti-rabbit IgG for 1 h. Finally, the samples were rinsed with TBS solution for multiple times, and dried in nitrogen gas before fluorescence imaging.

Results and discussion

Characterization of the ZnO NRs arrays

Scheme 1 illustrates fabrication processes of the ZnO NRs-based platform. A 200 nm Au-layer was first deposited on a Si substrate, followed by coating of a <002>-aligned ZnO seed layer (Fig. S1) of 100 nm thickness. A PMMA layer was subsequently spin-coated on top of the seed layer as mask, and selectively etched to expose the ZnO seed layer. The precise and patterned etching was carried out using electron-beam lithography, resulting in a matrix composed of aligned rectangular domains (Fig. S2). Each domain is 300 μm × 60 μm in size, consisting of 375×75 circular apertures of the same diameter. The apertures are evenly distributed to form an ordered array, with a center-to-center distance of the nearest neighbors of 800 nm. There are six types of domains: albeit the same lateral arrangement of apertures in each domain, the aperture size of each type is distinct (Fig. S3).

Next, the apertures asisted formation of arrays of vertically-standing single ZnO NRs. As demonstrated by the large-scale top-view SEM image (Fig. 1a), the resultant sample still maintained the matrix of rectangular domains. Within each rectangular domain, 375×75 single ZnO NRs were fabricated exclusively at the sites of the written apertures, showing identical diameter, height, orientation, and forming a highly-ordered uniform array (Fig. 1b–c). As shown in Fig. 1d–i, the *AZ* NRs within the same array possess an identical morphology, *i.e.* orderly-aligned typical hexagonal prisms with the same height and diameter, indicating the high crystalline quality and well-controlled growth of these NRs. Based on statistical analysis of SEM images, the average diameters of the NRs in *AZ1–AZ6* were ~150, 180, 230, 270, 320, and 410 nm, respectively (Fig. S4). The average NR heights of these arrays were ~1.4, 1.4, 1.3, 1.1, 1.0, and 1.0 μm, respectively. The lateral arrangement and density (numbers per unit area) of the NRs in all arrays are identical. It is noted that the smallest gap between the neighbouring NRs is ~390 nm, which is sufficient to avoid strong coupling with evanescent fields from the neighbouring NRs.[22] Such uniform arrays

Please do not adjust margins

Please do not adjust margins

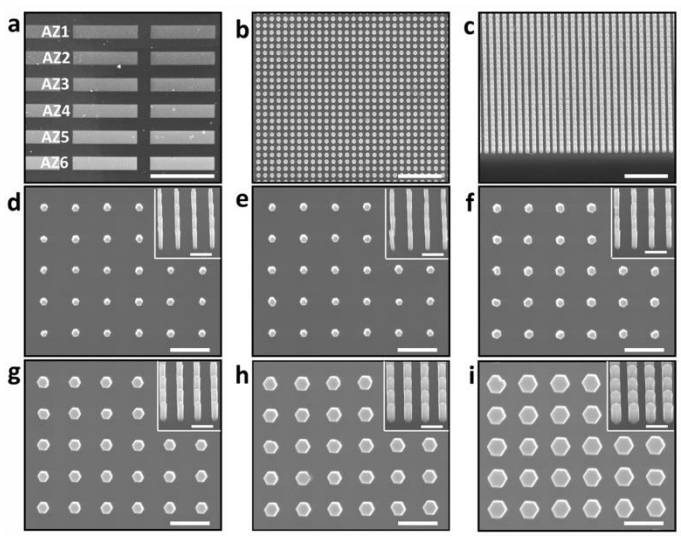

Fig. 1 (a) Top-view SEM image of six groups of ZnO-NRs arrays simultaneously fabricated on the same substrate (the scale bar is 300 μm). (b) Top- and c) 45°-tilt view of *AZ6*, presented as an example. (the scale bars are 5 μm). (d–i) High-resolution SEM images of the *AZ1*, *AZ2*, *AZ3*, *AZ4*, *AZ5*, and *AZ6* (the scale bars are 1 μm), where the corresponding 45° tilt-view images are presented in the insets (the scale bars are 1 μm).

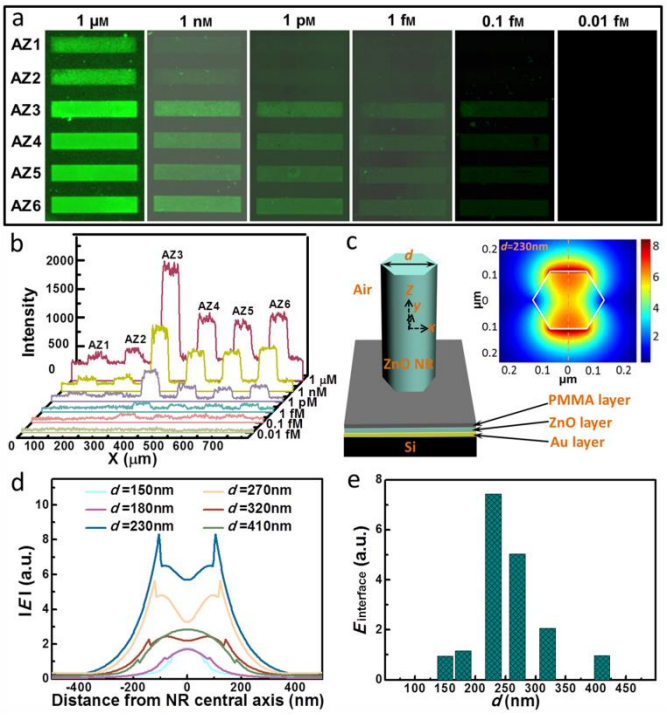

Fig. 2 (a) Fluorescent images and (b) fluorescence-intensity distribution of *AZ1–AZ6* arrays, treated by R6G solutions at various concentrations. The area of each array is 300 μm × 60 μm. (c) Configuration and calculated electric field |*E*| distribution on an *x*-*y* plane of a single *AZ* NR with *d* of 230 nm. (d) |*E*| along *y*-axis of the NRs and e) the evanescent field at the ZnO/air interface, with *d* of 150, 180, 230, 270, 320, and 410 nm.

with a range of NR diameters simultaneously formed on the same substrate provide an ideal prototype for quantitative analysis of *d*-dependent FE properties of individual ZnO NRs.

FE properties of the ZnO-NRs arrays

FE properties of the ZnO-NRs arrays were first evaluated using R6G (0.01 fM−1 μM) as the target fluorophore under an excitation centered at 530 nm (Fig. 2a). It is found that, for the given types of arrays, the detected fluorescence intensity decreased with the reduction of the R6G concentration. Excitingly, pronounced signal of R6G can be still observed from *AZ3*, *AZ4*, *AZ5*, and *AZ6* at a concentration as low as 0.1 fM. More importantly, the signal magnitude is evidently dependent on the *d* of the NRs. At all tested concentrations, *AZ3* provided the strongest signal. Quantitative analysis of the fluorescence intensity distribution (Fig. 2b) indicates that the intensity obtained from *AZ3* was approximately 4 fold that from *AZ1* and *AZ2*, and ~2 fold that from *AZ4*, *AZ5*, and *AZ6* arrays.

The surface area of the NRs determines the amount of R6G loaded, which will affect the detected fluorescence intensity. To quantitatively explore FE properties of the ZnO-NRs arrays, it is necessary to exclude this contribution originating from the increased surface area. To do so, we calculated the normalized fluorescence intensity (*I*/*A*) values of the different *AZ* arrays treated by 1 μM R6G solution (as summarized in Table S1, where *I* is the measured fluorescence intensity, *A* is the estimated surface area of a single ZnO NR with the NR approximated as a cylinder by referring the relevant *d* and NR height). For *AZ1–AZ6*, *I*/*A* is ~590, 610, 2040, 1110, 940, and 770 μm^{-2}, respectively. Evidently, *AZ3* showed the highest *I*/*A* among all the samples. Compared with *AZ1*, *AZ3* had only a 44% increased surface area, whilst its fluorescence intensity was approximately 400% enhanced. For *AZ6*, its surface area was 43% higher than that of *AZ3*, but its fluorescence intensity was 45% less than that of *AZ3*. Based on these results, it can be rationally concluded that, besides the surface area, *d* has remarkable influence on the FE properties of the NR platform.

To understand such *d*-dependent FE properties, FDTD simulations on the distribution of waveguide-induced electric field |*E*| were carried out (FDTD solutions 8.6). The *AZ* NRs were modelled referring to the real *AZ* NRs fabricated in this work, with all components, including the Si substrate, Au layer, ZnO layer, PMMA layer, the vertical hexagonal ZnO prism, and the surrounding medium (air) under consideration. The thicknesses of the Au, ZnO and PMMA layer in the model were set to be 200, 100 and 200 nm, respectively. The NRs height was fixed to be 1.5 μm, and the *d* values were 150, 180, 230, 270, 320, and 410 nm. Total-field scattered-field source with a radiation wavelength of 530 nm and polarizing along the *y*-axis was applied on the top of the NR with the incidence direction along the *z*-axis. The resultant |*E*| distribution on an *x*-*y* plane of the NR with *d* of 230 nm (Fig. 2c) showed significant evanescent field, evidently stronger than all the other NRs (Fig. S5). To quantitatively evaluate the evanescent field of the NRs with different *d*, |*E*| values of the *AZ1–AZ6* along the *y*-axis were plotted in Fig. 2d. It is found that, for the NRs with *d* of 150, 180, 320, and 410 nm, the maximum |*E*| value presents inside the NRs, whilst the evanescent field outside of the NRs is rather weak; in sharp contrast, the maximum |*E*| of the NRs with *d* of 230 and 270 nm locates outside of the NRs, resulting in a remarkable evanescent field surrounding the NRs. The simulated electric field at

This journal is © The Royal Society of Chemistry 20xx

Please do not adjust margins

the ZnO/surrounding-medium interface of the NRs (denoted as $E_{interface}$) is shown in Fig. 2e. Consistently, the $E_{interface}$ of the NR with *d* of 230 nm is highest among all NRs: ~40% and ~200% higher than those with *d* of 270 and 320 nm, and even ~600% higher than the NR with *d* of 150, 180 and 410 nm. It is worth noting that the height of the *AZ* NRs could also influence the evanescent field. According to the FDTD simulations, when varying the NR height from 1.5 to 1.4, 1.3, 1.2, 1.1, and 1.0 μm while keeping *d* of 230 nm, only a small difference less than 5.5% was observed for the average $E_{interface}$ value (Table S2). The results indicate that the influence of the NR height (in the NR height range applied in this work) on the evanescent field is much weaker than that of the NR diameter (Fig. 2e). Such *d*-dependent evanescent field supports the experimental observations on the *d*-dependent FE performance well.

FE properties of the NRs without the pre-deposited Au layer (denoted as "*Z*" NRs) were also studied (details in the supporting information). Both experimental and theoretical results revealed that the *Z* NRs present similar *d*-dependent FE properties to those of the *AZ* but with largely reduced $E_{interface}$ and *I* (Fig. S6–S8), indicating that the Au layer as the substrate can afford much higher FE than the Si substrate. For example, after treated by R6G solutions, the *Z3* NRs have approximately the same diameter, height, and lateral arrangement to the case in the presence of Au substrate, *i.e. AZ3* NRs, but present much weaker fluorescence signal (Fig. 3a). Since the thickness of the ZnO seed layer and the remaining PMMA layer are much larger than the required metal-fluorophore coupling distance (usually < 20 nm), metal enhanced fluorescence effect cannot influence the FE properties of *AZ* arrays. This is further confirmed by the nearly same fluorescence lifetime of the R6G on the ZnO NRs in the presence/absence of the Au layer (Fig. S9). Rationally, the contribution of the Au layer can be assigned to: (1) reducing the absorption of the Si substrate upon both the excitation and the emission light (Fig. S10); (2) enhancing waveguiding properties of the ZnO NRs by providing a reflecting mirror.[30] Combing the contribution of high-order waveguide modes of NRs and the Au layer, the detected fluorescence intensity of R6G on *AZ3* was ~300 fold as that on glass substrate (Fig. 3b), which is higher than all the reported results of ZnO-based FE platforms without surface modification.[33,53]

Detection of cancer biomarker CEA

In order to demonstrate the practical application potential of the *AZ* arrays as FE platforms, a widely used sandwich immunoassay method for fluorescence-based detection of cancer biomarker CEA was applied.[54] Briefly, GPTS was used to modify the surface of the *AZ* arrays and introduce active epoxy groups for immobilization of the capture antibody. The three additional peaks located at 2921, 2852, and 1461 cm^{-1} in the FTIR spectrum of the GPTS-modified ZnO NRs relative to the spectrum of the pristine NRs (Fig. S11) confirm the GPTS modification.[42] Next, detection of CEA at various concentrations was performed by using CEA-mAb as the capture antibody, CEA-pAb as the recognition antibody, Cy3-labelled anti-rabbit IgG as the fluorescein-labelled secondary antibody, together with BSA to eliminate the non-specific binding of proteins (Scheme 1). SEM images reveal that such fabrication procedure for the CEA detection leaded to the formation of a uniform coating layer with an average thickness of ~90 nm on the NRs (Fig. 4a–c).

The obtained fluorescent images and fluorescence-intensity distribution of Cy3 molecules on the *AZ* arrays, as well as the

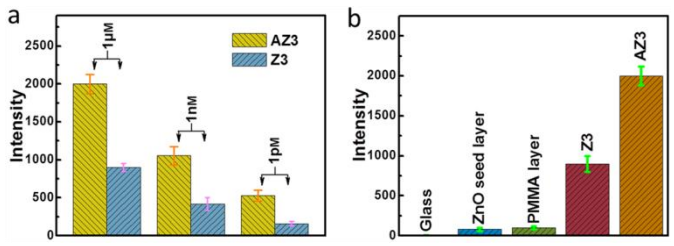

Fig. 3 (a) Fluorescence intensity of the *AZ3* and *Z3* samples treated by 1 μM, 1 nM and 1 pM R6G solutions. (b) Comparison of fluorescence intensity collected from different platforms, including glass, the ZnO seed layer on Si, the PMMA layer on Si, Z3 arrays, and AZ3 arrays, treated by 1 μM R6G solution.

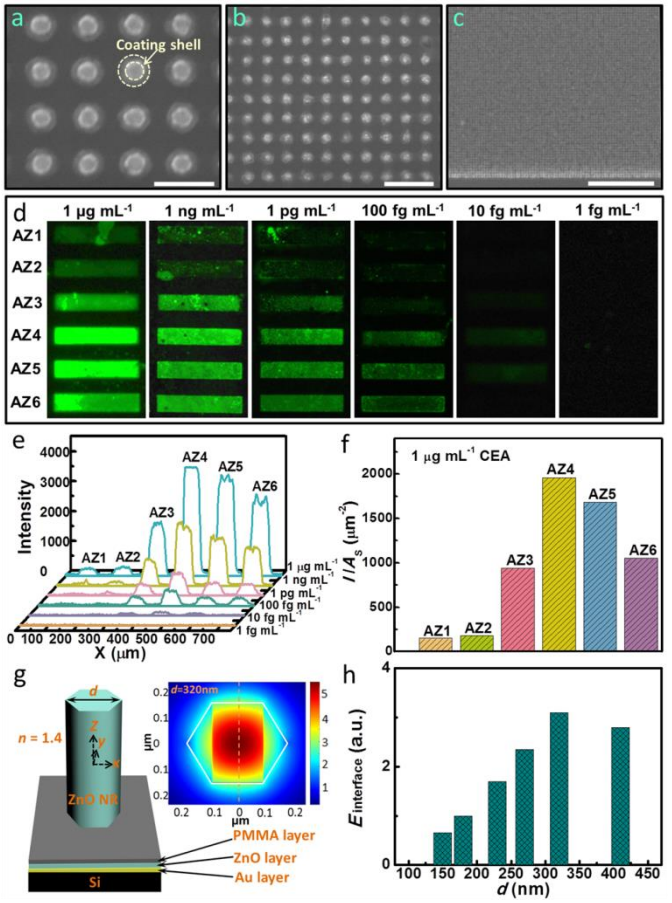

Fig. 4 (a–c) SEM images of the *AZ* array for CEA detection (the scale bars are respectively 1 μm, 2 μm, and 20 μm). (d) Fluorescent images and (e) fluorescence-intensity distribution of Cy3 molecules on the FE platform, where a sandwich immunoassay method was used to realize fluorescence-based detection of CEA at various concentrations. (f) The ratio of the measured fluorescence intensity to the estimated surface area of the coating shell on a single NR (I/A_S). (g) Calculated electric field $|E|$ distribution on an *x*-*y* plane of the NR with *d* of 320 nm and surrounding medium of *n* =1.4. (h) The evanescent field at the ZnO/surrounding-medium interface of the NRs with *d* of 150, 180, 230, 270, 320, and 410 nm.

Please do not adjust margins

measured fluorescence intensity as a function of CEA concentration are presented in Fig. 4d, 4e and S12, respectively. By referring 3-fold standard deviations above the background (Fig. S13), the LOD for CEA detection was deduced to be 10 fg mL^{-1}, which is one order of magnitude improved than the best results using fluorescence-based detection methods ever reported.[42,43,53–55] The results indicate the great promise of these *AZ* arrays for bioassays. Interestingly, at all given CEA concentrations, the strongest fluorescence intensity was obtained from *AZ4* instead of *AZ3* in this case. To figure out the underlying reason, the surface area was first considered since it determines the load of Cy3 (CEA). The ratio of the measured Cy3 fluorescence intensity (I) to the estimated surface area of the coating shell on a single NR (A_S) treated by 1 μg mL^{-1} CEA solution was calculated. Given A_S of *AZ1–AZ6* is ~1.63, 1.79, 1.92, 1.84, 1.91, and 2.29 μm^2, I/A_S was deduced to be ~150, 180, 940, 1960, 1680, and 1050 μm^{-2}, respectively (Fig. 4f). Notably, the A_S value of *AZ4* was only ~20% higher than that of *AZ1*, while its intensity was ~13 fold higher than that of *AZ1*, resulting in an I/A_S value more than one order of magnitude higher than that of *AZ1*.

Given the facts that changing the refractive index (n) around the ZnO NR can affect the waveguiding properties and the n of the coating shell should be larger than that of air (1.0), we then explored the influence of n of the surrounding medium, using FDTD simulations. It is revealed that, for the waveguide-induced $|E|$ distributions of the *AZ* NRs with the surrounding medium of n =1.4, the maximum evanescent field was obtained from the NR with d of 320 nm (Fig. 4g–4h and S14). Albeit the small variation from experimental results due to the more complicated factors involved in the experimental configuration of the platform, the simulation results indicate the same trend, *i.e.* the strongest evanescent field was generated from the *AZ* with a larger d when applying surrounding medium with a higher n. These results further confirm that the high-order waveguide modes contribute primarily to the FE properties of the ZnO NRs-based platform. Moreover, it is revealed that by adjusting the surrounding medium high-order waveguide mode-induced FE performance can be effectively tuned.

Conclusions

In conclusion, by simultaneously fabricating well-aligned and patterned ZnO NR arrays with six different d on a same substrate, d-dependent FE properties have been systematically explored, combining experimental measurements with theoretical simulation. The results indicate that high-order waveguide modes, which are strongly dependent on the NR diameter, substrate, and surrounding medium, can enhance the NR-based FE performance significantly, beyond the contribution of an increased surface area alone. By using optimized NRs arrays as the FE platform, a superlow LOD of 0.1 fM for R6G detection and 10 fg mL^{-1} for Cy3-based CEA detection have been achieved. The latter is one order of magnitude improved than the best reported results using fluorescence-based detection.

Moreover, the FE performance of the ZnO NRs-based platform has the potential to be further boosted. (1) The positive contribution of evanescent field coupling on FE of ZnO NRs has been theoretically suggested previously.[52] To demonstrate the effect of high-order waveguide modes exclusively without disturbance of the evanescent field coupling,[51] relatively large gaps among the neighboring NRs were employed in this work. Apparently, reducing the gap between the neighboring NRs would increase the surface area of the platform and the evanescent field coupling, which both promote the detection sensitivity. (2) Further incorporating with fluorescent probes owning selective detection capability would also reinforce the properties of the FE biochip. (3) By further tuning the NRs length, the polarization state of the used excitation, and the reflectance of the pre-deposited metal film, the ZnO-NRs arrays platform would also upgrade the capability for ultrahigh sensitive and multi-target detection.

Conflicts of interest

There are no conflicts to declare.

Acknowledgements

This work is financially supported by the National Natural Science Foundation of China (51772066, 21473045, 11674387, 61390503, 11574385), Natural Science Foundation of Heilongjiang Province, China (E2015003), Ministry of Science and Technology of China (2016YFA0200800, 2016YFA0200400), and Key Research Program of Frontier Sciences, CAS (QYZDJ-SSW-SLH042).

References

1 M. P. Landry, H. Ando, A. Y. Chen, J. Cao, V. I. Kottadiel, L. Chio, D. Yang, J. Dong, T. K. Lu and M. S. Strano, *Nat. Nanotechnol.*, 2017, **12**, 368–377.
2 S.-E. Kim, S. D. Jo, K. C. Kwon, Y.-Y. Won and J. Lee, *Adv. Sci.*, 2017, **4**, 1600471.
3 H. Xiong, H. Zuo, Y. Yan, G. Occhialini, K. Zhou, Y. Wan and D. J. Siegwart, *Adv. Mater.*, 2017, **29**, 1700131.
4 M. Singh, A. Alabanza, L. E. Gonzalez, W. Wang, W. B. Reeves and J. Hahm, *Nanoscale*, 2016, **8**, 4613–4622.
5 B. Koh, X. Li, B. Zhang, B. Yuan, Y. Lin, A. L. Antaris, H. Wan, M. Gong, J. Yang, X. Zhang, Y. Liang and H. Dai, *Small*, 2016, **12**, 457–465.
6 N. H. T. Tran, K. T. L. Trinh, J.-H. Lee, W. J. Yoon and H. Ju, *Small*, 2018, **14**, 1801385.
7 R. Viter, M. Savchuk, N. Starodub, Z. Balevicius, S. Tumenas, A. Ramanaviciene, D. Jevdokimovs, D. Erts, I. Iatsunskyi and A. Ramanavicius, *Sens. Actuators B*, 2019, **285**, 601–606.
8 L. Liu, D. Shan, X. Zhou, H. Shi, B. Song, F. Falke, A. Leinse and R. Heideman, *Biosens. Bioelectron.*, 2018, **106**, 117–121.
9 H. Yousefi, M. M. Ali, H.-M. Su, C. D. M. Filipe and T. F. Didar, *ACS Nano*, 2018, **12**, 3287–3294.
10 L. Wu and X. Qu, *Chem. Soc. Rev.*, 2015, **44**, 2963–2997.
11 Z. Zheng, W.-C. Geng, J. Gao, Y.-Y. Wang, H. Sun and D.-S. Guo, *Chem. Sci.*, 2018, **9**, 2087–2091.
12 Y. Park, Y.-M. Ryu, Y. Jung, T. Wang, Y. Baek, Y. Yoon, S. M. Bae, J. Park, S. Hwang, J. Kim, E.-J. Do, S.-Y. Kim, E. Chung, K. H. Kim, S. Kim and S.-J. Myung, *ACS Nano*, 2014, **8**, 8896–8910.
13 A. B. Chinen, C. M. Guan, J. R. Ferrer, S. N. Barnaby, T. J. Merkel and C. A. Mirkin, *Chem. Rev.*, 2015, **115**, 10530–10574.
14 M. Gao, F. Yu, C. Lv, J. Choo and L. Chen, *Chem. Soc. Rev.*, 2017, **46**, 2237–2271.

This journal is © The Royal Society of Chemistry 20xx

Please do not adjust margins

Please do not adjust margins

15 D. Yang, H. Wang, C. Sun, H. Zhao, K. Hu, W. Qin, R. Ma, F. Yin, X. Qin, Q. Zhang, Y. Liang and Z. Li, *Chem. Sci.*, 2017, **8**, 6322–6326.
16 R. Zhang, L. Liang, Q. Meng, J. Zhao, H. T. Ta, L. Li, Z. Zhang, Y. Sultanbawa and Z. P. Xu, *Small*, 2019, **15**, 1803712.
17 J. Sun, R. Malishev, A. Azoulay, J. Tzadikov, M. Volokh, R. Jelinek and M. Shalom, *Small*, 2018, **14**, 1800516.
18 W. Zheng, S. Zhou, J. Xu, Y. Liu, P. Huang, Y. Liu and X. Chen, *Adv. Sci.*, 2016, **3**, 1600197.
19 K. Lei, M. Sun, L. Du, X. Zhang, H. Yu, S. Wang, T. Hayat and A. Alsaedi, *Talanta*, 2017, **170**, 314–321.
20 O. Adegoke, M.-W. Seo, T. Kato, S. Kawahito and E. Y. Park, *Biosens. Bioelectron.*, 2016, **86**, 135–142.
21 X. Chen, X. Zhang, L.-Y. Xia, H.-Y. Wang, Z. Chen and F.-G. Wu, *Nano Lett.*, 2018, **18**, 1159–1167.
22 P. Liu, Y. Zhou, M. Guo, S. Yang, O. Félix, D. Martel, Y. Qiu, Y. Ma and G. Decher, *Nanoscale*, 2018, **10**, 848–855.
23 Y. Kim, B. Kang, H.-Y. Ahn, J. Seo and K. T. Nam, *Small*, 2017, **13**, 1700071
24 V. Flauraud, R. Regmi, P. M. Winkler, D. T. L. Alexander, H. Rigneault, N. F. van Hulst, M. F. García-Parajo, J. Wenger and J. Brugger, *Nano Lett.*, 2017, **17**, 1703–1710.
25 X. Liu, S. P. McBride, H. M. Jaeger and P. F. Nealey, *Nanotechnology*, 2016, 27, 285301.
26 A. Puchkova, C. Vietz, E. Pibiri, B. Wünsch, M. S. Paz, G. P. Acuna and P. Tinnefeld, *Nano Lett.*, 2015, 15, 8354-8359.
27 J.-M. Jung, H.-W. Yoo, F. Stellacci and H.-T. Jung, *Adv. Mater.* 2010, **22**, 2542–2546.
28 N. Akhtar, S. K. Metkar, A. Girigoswami and K. Girigoswami, *Mater. Sci. Eng. C*, 2017, **78**, 960–968.
29 A. Peer, Z. Hu, A. Singh, J. A. Hollingsworth, R. Biswas and H. Htoon, *Small*, 2017, **13**, 1700660.
30 Y. Yin, Y. Sun, M. Yu, X. Liu, T. Jiang, B. Yang, D. Liu, S. Liu and W. Cao, *Sci. Rep.*, 2015, **5**, 8152.
31 Z. Mei and L. Tang, *Anal. Chem.*, 2017, **89**, 633–639.
32 C. Xie, L. Hanson, Y. Cui and B. Cui, *Proc. Natl. Acad. Sci. USA*, 2011, **108**, 3894–3899.
33 C. Liu, F. Meng, W. Zheng, T. Xue, Z. Jin, Z. Wang and X. Cui, *Sens. Actuators B*, 2016, **228**, 231–236.
34 S. M. Wells, I. A. Merkulov, I. I. Kravchenko, N. V. Lavrik and M. J. Sepaniak, *ACS Nano*, 2012, **6**, 2948–2959.
35 M. Kandziolka, J. J. Charlton, I. I. Kravchenko, J. A. Bradshaw, I. A. Merkulov, M. J. Sepaniak and N. V. Lavrik, *Anal. Chem.*, 2013, **85**, 9031–9038.
36 D. Verardo, F. W. Lindberg, N. Anttu, C. S. Niman, M. Lard, A. P. Dabkowska, T. Nylander, A. Månsson, C. N. Prinz and H. Linke , *Nano Lett.*, 2018, **18**, 4796–4802.
37 J. Hahm, *J Nanosci Nanotechnol.*, 2014, **14**, 475–486.
38 J. Hahm, *Annu. Rev. Phys. Chem.*, 2016, **67**, 691–717.
39 A. Dorfman, N. Kumar and J. Hahm, *Adv. Mater.* 2006, **18**, 2685–2690.
40 A. Tereshchenko, M. Bechelany, R. Viter, V. Khranovskyy, V. Smyntyna, N. Starodub and R. Yakimova, *Sens. Actuators B*, 2016, **229**, 664–677.
41 T. Wang, J. Costan, A. Centeno, J. S. Pang, D. Darvill, M. P. Ryan and F. Xie, *J. Mater. Chem. C*, 2015, **3**, 2656–2663.
42 W. Hu, Y. Liu, T. Chen, Y. Liu and C. M. Li, *Adv. Mater.*, 2015, **27**, 181–185.
43 L. Guo, Y. Shi, X. Liu, Z. Han, Z. Zhao, Y. Chen, W. Xie and X. Li, *Biosens. Bioelectron.*, 2018, **99**, 368–374.
44 C.-H. Sang, S.-J. Chou, F. M. Pan and J.-T. Sheu, *Biosens. Bioelectron.* 2016, **75**, 285–292.
45 S. Chu, G. Wang, W. Zhou, Y. Lin, L. Chernyak, J. Zhao, J. Kong, L. Li, J. Ren and J. Liu, *Nat. Nanotechnol.*, 2011, **6**, 506–510.
46 A. Manekkathodi, Y.-J. Wu, L.-W. Chu, S. Gwo, L.-J. Chou and L.-J. Chen, *Nanoscale*, 2013, **5**, 12185–12191.
47 R. Yan, D. Gargas and P. Yang, *Nat. Photonics*, 2009, **3**, 569–576.
48 M. Singh, S. Song and J. Hahm, *Nanoscale*, 2013, **6**, 308–315.
49 J. Truong, M. Singh, M. Hansen and J. Hahm, *Nanoscale*, 2017, **9**, 8164–8175.
50 D. J. Sirbuly, A. Tao, M. Law, R. Fan and P. Yang, *Adv. Mater.*, 2007, **19**, 61–66.
51 S. Börner, C. E. Rüter, T. Voss, D. Kip and W. Schade, *Phys. Status Solidi A*, 2007, **204**, 3487–3495.
52 T. Wang, A. Centeno, D. Darvill, J. S. Pang, M. P. Ryan and F. Xie, *Phys. Chem. Chem. Phys.*, 2018, **20**, 14828–14834.
53 J. Kim, S. Kwon, J.-K. Park and I. Park, *Biosens. Bioelectron.*, 2014, **55**, 209−215.
54 W. Qin, K. Wang, K. Xiao, Y. Hou, W. Lu, H. Xu, Y. Wo, S. Feng and D. Cui, *Biosens. Bioelectron.*, 2017, **90**, 508−515.
55 W. Hu, Y. Liu, H. Yang, X. Zhou and C. M. Li, *Biosens. Bioelectron.*, 2011, **26**, 3683−3687.
56 Y. Yin, Y. Sun, M. Yu, X. Liu, B. Yang, D. Liu, S. Liu, W. Cao and M. N. R. Ashfold, *RSC Adv.*, 2014, **4**, 44452−44456.
57 J. M. Lee, Y.-S. No, S. Kim, H.-G. Park and W. I. Park, *Nat. Commun.*, 2015, **6**, 6325.

This journal is © The Royal Society of Chemistry 20xx

Please do not adjust margins